SSC09-VII-2

Autonomous Pose Estimations for In-Orbit Self-Assembly of Intelligent Self-Powered Modules

Samia Smail, David S. Wokes, Craig I. Underwood and Phil L. Palmer
Surrey Space Centre
University of Surrey, Guildford, Surrey, GU2 7XH.
S.Smail@surrey.ac.uk, D.Wokes@surrey.ac.uk, C.Underwood@surrey.ac.uk, P.Palmer@surrey.ac.uk

ABSTRACT

The ability to autonomously determine the position and attitude of a swarm of satellites is a promising way of assembling Intelligent Self-powered Modules (ISMs) in orbit. This self assembly is guided through simple actuators and sensors and requires fewer resources. A vision based system is used to determine the pose of ISMs attempting docking, through two strategies: Spheroid modeling and feature detection methods. The former technique takes an image of the ISM to reconstruct its position. An additional set of reflectors are placed on each facet to then determine the attitude of the ISM. The attitude algorithms developed are validated for distances up to 30m, with the position determination tested for distances up to 50m. These methods are combined to autonomously estimate the pose of an ISM attempting to dock with a coupled structure of previously launched and connected ISMs.

INTRODUCTION

Space technology is heading towards small, light and cost effective satellites, however, a number of space missions require large structures to complete their operating goals. Thereby the concept of launching modular spacecraft and assembling them in the desired configurations, once in orbit, is becoming significantly important[1]. Of particular interest is the ability to perform such an operation autonomously, especially when satellites suffer from bandwidth limitations and communication dropouts. Since 1987, when the Kvant-1 module was launched for docking with the base module of the Mir Station, assembly in space included human-in-the-loop operations to complete safe assembly of spacecraft[2]. However, the success of the Jules-Verne mission has opened the door for autonomous Rendezvous and Docking (RVD) operations[3]. One of the crucial phases of this autonomy is the estimation of the relative pose of the satellites attempting docking.

Possible technologies and techniques have been developed for such a purpose. In general, the object being tracked is identified using a number of sensors that provide the necessary information to estimate the relative pose. IGLA[4] and KURS[5] are radiofrequency systems developed to guide Soyuz and Progress during the RVD phases with Salyut, Mir and the International Space Station (ISS). However, these RF systems consume a large amount of power and require large antennas, as well as robust techniques to overcome the disturbances at closer ranges.

A range of sensors have been proposed for guiding the Crew Exploration Vehicle during its proximity operations. The Advanced Video Guidance Sensor (AVGS)[6] flew on DART and Orbital Express. It uses processed data from an imaging sensor, integrated laser sources and narrow-band-filtered retro-reflective targets to estimate the relative state between two spacecraft operating in close proximity. The Automatic Targeting and Reflective Alignment Concept (AutoTRAC)[7] is a computer vision system that processes two images to locate the reflectors on the target satellite and then compares the output with the predefined configuration of the object being tracked. The Natural Feature Image Recognition (NFIR)[7] system eliminates the need for reflectors, and instead compares the 3D model of the target with the boundary of the images being captured. The Optech LIDAR[7] sensor obtains range measurements by sending laser pulses on the target's reflective surface.

In a three month mission, DARPA's Orbital Express demonstrated the feasibility of accomplishing an autonomous in orbit refuelling and servicing using a robotic manipulator. The Autonomous Rendezvous and Capture Sensor System (ARCSS) along with its vision based software (Vis-STAR), guided the satellites during

the rendezvous and berthing phases[8]. As mentioned above, the AVGS also assisted in the proximity operations of this mission. Recently, the automated transfer vehicle used its on-board high precision navigation system to complete a rendezvous trajectory towards the ISS and automatically dock with its Zvezda module. Fine alignments were achieved through a videometre and a laser-type sensor[9].

This paper deals with estimating the relative pose of the Intelligent Self-powered Modules (ISMs) during the proximity operations. The relative positions of the modules are determined using both disc reconstruction and spherical modelling algorithms, based upon coloured features on the target. Independently, an L-shaped set of reflectors is used to determine the relative orientation. After describing in greater detail the ISM mission concept, the pose determination techniques are described, followed by an analysis on the accuracy of these techniques. The theory is then validated through multiple simulations, before concluding with a discussion on the practicality of the methods developed.

INTELLIGENT SELF-POWERED MODULES

The ISM mission concept is to decompose a large monolithic spacecraft into a group of smaller satellites, each responsible for their designated functions (i.e. propulsion, attitude control, communication, upgrading payloads and scientific instruments). Such a modular architecture allows straightforward interchangeability, upgrading and maintenance in orbit, at lower costs. Once in orbit, the ISMs autonomously search, navigate, capture and dock, to achieve the configuration required for completing a specific mission.

The Electromagnetic Flat Docking System (EFDS), with its simple sensors and actuators, direct the ISMs to self assemble without damaging the sensitive components of the neighbouring satellites[10]. As it requires power from batteries only, the ISMs can configure and reconfigure without the need to consume extra propellant.

Figure 1 shows the ISM architecture. It consists of three main parts:

- The core: a cubic structure that contains all the satellite's main subsystems.
- The EFDS: cuboid housings mounted on the six sides of the ISM core.
- Solar cells: covers the rest of the ISM's non-axial facets

Some of the possible applications of the ISM mission include constructing magnetic shielding[11], large telescopic mirrors[12], and large solar panels[13].

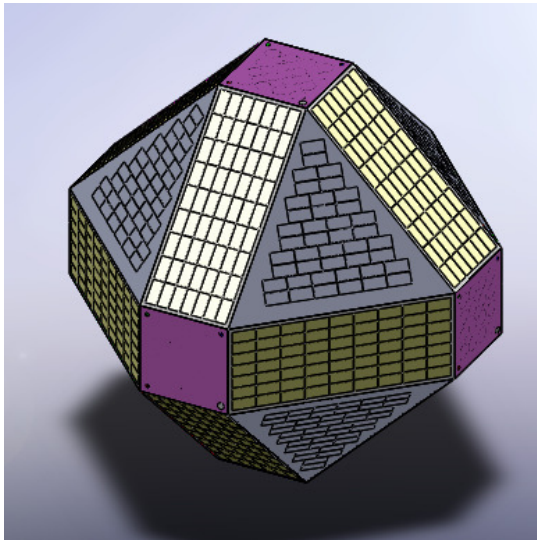

Figure 1: ISM Body Structure

One mission scenario can consist of a mother craft that acts as the core of the cluster, with a number of additional ISMs that define the housekeeping payload of the whole structure. The mother craft is equipped with all the necessary electronics to provide the required control of the cluster and it is supported with additional equipment from the rest of the ISM structure.

In this paper, one ISM approaches a cluster of eight docked ISMs, in order to rendezvous and dock in the remaining place. The specific docking technique is not covered in this discussion[12].

AUTONOMOUS POSE ESTIMATION

Relative Position Estimation

From a computer's point of view, a picture of a spacecraft structure can be hard to break down if the different parts of that structure do not have unique features. In our case, if we are dealing with just a single ISM and assume that any pixel above an intensity threshold is identified as the target structure, then this is not a problem. But, when two or more ISMs are present in the picture, this process becomes more challenging. Moreover, occlusion can occur between one ISM and another and noise can give false positives. To tackle target identification, the primary facets on each ISM are coloured purple, to distinguish them from the solar panels and, after image erosion, background noise. Each ISM has six square-faced facets along its primary axes. These facets make up the EFDS and each facet has two additional features on them, as shown in figure 2.

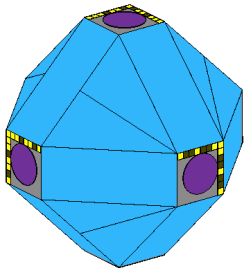

Figure 2: ISM Body Structure

The 'L' shaped reflector system will be used for accurate attitude determination and is described in the next section. The centre circle is coloured solely for position determination purposes.

A method of identifying the position and attitude estimate of an ISM structure was derived and discussed by Wokes, Smail *et al.*[14], where specific structures were considered at distances from 5m up to 100m. There was also an assumption that each ISM's EFDS were uniquely colour-coded. This meant that, for each EFDS facet that was detected in an image, it could immediately be assigned to the appropriate ISM to which its colour corresponded to. If this colour-scheme is removed and each ISM becomes identical in appearance, the pose estimation problem simultaneously becomes simpler and more prone to errors. In this paper, we develop the aforementioned concepts for when a single ISM structure is being viewed. The focus of this section is on determining the position alone; attitude estimates can be extracted from these methods[14], but exact attitude determination is discussed in the next section.

When a circle / disc is projected onto a plane it yields an ellipse (As described by Semple and Kneebone[15]). From an ellipse on an image plane, it is possible to reconstruct two possible solutions for the position and orientation (direction of the normal vector) of a disc, with a given size. These solutions are easiest to visualize if we consider the reconstruction of a disc from its projection onto a sphere (see Wokes and Palmer[16]), where the equations describe a position vector $\vec{q}$ to the centre of the reconstructed disc and a vector normal to the surface of that disc, denoted by $\vec{p}$. These expressions can be extracted from spheroid reconstruction equations, given by

$$\vec{q} = \frac{\cos\beta}{\cos\alpha} S\vec{C}_{(1)} + \pm_1 \sin\beta . M\vec{C}_{(2)} \qquad (1)$$

$$\vec{p} = \pm\left\{ \sin\beta \frac{T}{\sqrt{B^2 - A^2}} \vec{C}_{(1)} + \pm_1 \sin\beta G\vec{C}_{(2)} \right\} \qquad (2)$$

Where:

$$S = \sqrt{A^2 + B^2 \cot^2\alpha}$$

$$M = \sqrt{\tan^2\alpha - \tan^2\beta}.\mathrm{T}$$

$$T = \sqrt{B^2 \cot^2\alpha - A^2 \cot^2\beta}$$

$$G = \frac{\sqrt{\cot^2\beta - \cot^2\alpha}\sqrt{B^2 + A^2\tan^2\alpha}}{\sqrt{B^2 - A^2}}$$

In the above expressions, α denotes the semi-major axis of the image sphere ellipse and β the semi-minor axis. A describes the half-length of the spheroid along its axis of symmetry and B the half-length of the spheroid along its degenerate axes. The column vectors $\vec{C}_{(i)}$ are taken from the rotation matrix from the camera frame to the image sphere ellipse frame; $\vec{C}_{(1)}$ points through the centre of the image sphere ellipse, $\vec{C}_{(2)}$ points in the direction of the ellipse's semi-major axis and $\vec{C}_{(3)}$ points in the direction of the ellipse's semi-minor axis. One can see through the structure of these equations, that the reconstructed solutions of the spheroid's position and orientation are therefore symmetric, through the $\vec{C}_{(1)}$-$\vec{C}_{(3)}$ plane. This is shown in figure 3.

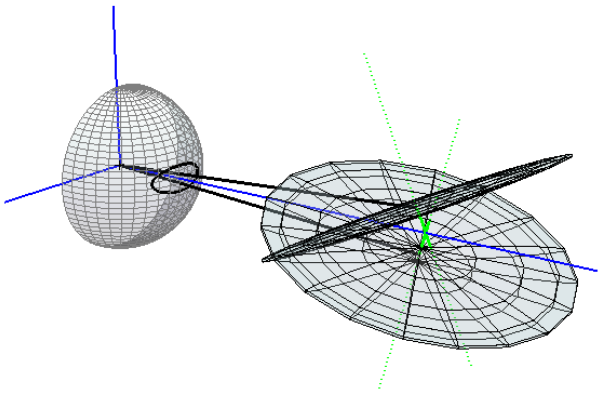

Figure 3: The reconstruction of a known spheroid or disc from its projection yields two solutions: the position vectors (black) and attitude vector (green) are reflections through the axes of the ellipse's centre-vector and semi-minor axis.

We will be using these equations in the degenerate sense: when $A \to 0$ the expressions describe the reconstruction of a disc, as shown in figure 3 – this is how we model the circles on the EFDS facets. One can also note there is degeneracy in the sign of $\vec{p}$, the normal vector to the disc. However, the negative solution will be pointing towards the camera. Hence if we define the normal to the EFDS to be pointing inwards, towards the centre of that ISM (and therefore away from the camera), then the analytic expression for the ISM's centre with respect to the camera frame is given by

$$\vec{Q}_{ism} = \vec{q} + \frac{1}{2}\lambda\vec{p} \qquad (3)$$

We define $\frac{1}{2}\lambda$ as the distance from the centre of the ISM to the EFDS surface, whilst $\vec{p}$ always takes the positive solution.

The reasoning for painting a disc onto each facet of the ISM is now clear; for each disc that is visible from the camera's perspective, an ellipse will be detected on the image plane. For each ellipse detected, two possible discs can be reconstructed in the 3-D space – one will accurately describe the facet, the other will be pointing in the wrong direction. For each reconstructed facet, there is an associated normal vector and the centre of each ISM lies along that normal vector – in the direction away from the camera. Because we know the size of the disc and the ISM, we obtain a position estimate of the ISM centre, from each detected disc. We also obtain a 'false' position estimate, given by the second reconstruction of the disc. The removal of the false solution is considered next.

For each facet that is detected, we obtain two possible centres for the ISM, whose values diverge away from each other the greater the eccentricity of its elliptic projection on the image. Each possible centre can then be represented as a sphere, which bounds that ISM. If these spheres are then re-projected down onto the image plane, they will yield ellipses. Where one ellipse will appear to bound the entire ISM on the image (assuming an accurate facet detection), the second ellipse will only partially bound the ISM – see figure 4. Hence, the algorithm we use for determining which ISM centre is the correctly estimated centre, projects the two sphere possibilities and counts the number of pixels inside each ellipse which have also been recognized as part of the overall target. Whichever ellipse has the greatest overlap is then selected as the true solution.

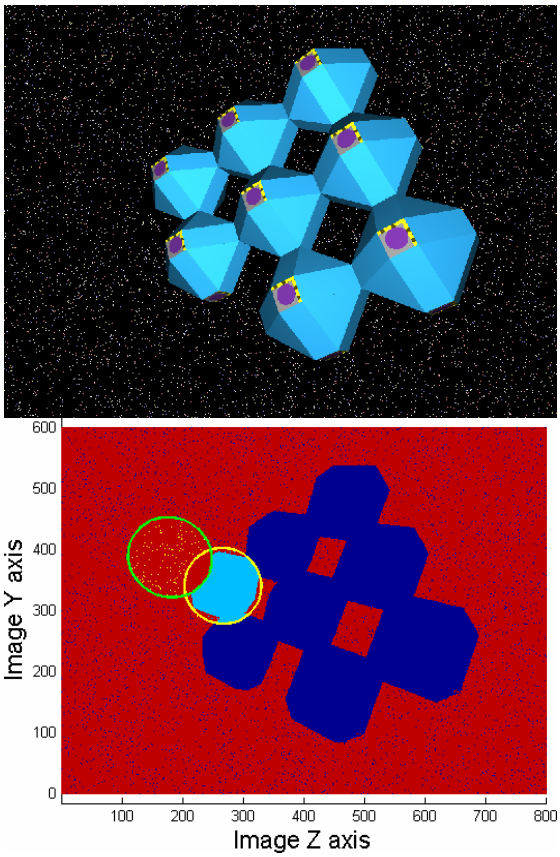

Figure 4: When a facet is detected (upper left corner), the ISM centre can be reconstructed in two positions and its bounding sphere re-projected onto the image plane (bottom). The ellipse with a sufficiently less intersection (green) with the original image is deemed the false solution.

For any ISM, the number of facets detected can vary between 0 and 3, depending upon the orientation, distance and occlusion. Without doing any analysis beforehand, there is no way to distinguish which ellipses that are detected correspond to which ISMs; for example, two discs with the same orientation will not be projected to equally oriented ellipses. As such, each detected disc projection is considered separately at first: upon bounding the projection with an ellipse, the two ISM centre solutions are reconstructed. Then, it is checked to see if the projection of the centre alone intersects with a candidate pixel that is above a chosen threshold - implying that it may be part of the ISM structure. If both solutions are, the projections of both spheres are calculated, as described above, then its pixellated ellipse found (for superposing onto the captured image). The intersection of such a pixellated ellipse and the pixels that have been identified as candidates for the ISM structures are counted for each solution: if there is a dramatically higher intersection for one over the other then the false solution has been

identified and can be removed. If there is still doubt, there is a final check that can be implemented. Because we are rendezvousing with a single structure of ISMs, the axes of all ISMs will be aligned – either parallel or perpendicular – with respect to each other. If there is still doubt in which solution to choose when reconstructing a disc, the normal vectors are then considered. This is shown in figure 5, where the black vectors denote the orientations that were reconstructed 'in confidence' (by the previous methods), whereas the red vector couplets are those in doubt. Where one of the red vector couplets should be closely aligned with the black vectors, the other may not. The one which isn't is then removed as a false solution. The cost function applied to each of the couplets is given by

$$J_i = \sum_{j \neq i}^{confirmed} (1 - (\vec{p}_i \cdot \vec{p}_j)^2)(\vec{p}_i \cdot \vec{p}_j)^2 \qquad (4)$$

where the sum ranges over all 'confirmed' orientation estimates. The above expression is, essentially, measuring the double-angle between the vectors $\vec{p}_i$ and $\vec{p}_j$. That way, the sum lies between 0 and 1. Furthermore, if the angles are either 0 or 90 degrees, the cost for that product is zero. The vector in the couplet with the smallest value of J_i is selected as the 'true' solution. The vector with greater value, is discarded.

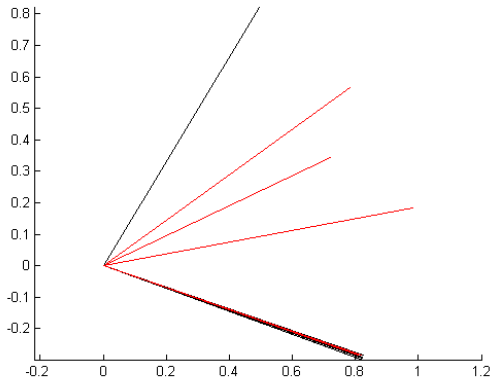

Figure 5: From each disc projection there are two possible normal vectors reconstructed. The ambiguous reconstruction pairs (red) are compared with those that are reconstructed with confidence (black). Whichever normal is better aligned with the black vectors, is deduced as the correct reconstruction.

Now that a collection of ISM centres has been obtained, there remains the task of correctly grouping those centres. We now derive the ISM's radial error term, as a result of inaccuracies in α and β. Using equations (1) and (2) for the reconstructed position $\vec{q}$ and orientation $\vec{p}$ of a disc, the squared magnitude R_{ISM} of the ISM centre $\vec{Q}_{ISM}$ is calculated:

$$R_{ISM}(\alpha,\beta)^2 = \frac{B^2}{\sin^2\alpha}\mathrm{H} + \frac{\lambda^2}{4} + \frac{\lambda B \sin\beta\cos\beta}{\sin^2\alpha}\mathrm{N} \qquad (5)$$

Where:

$$\mathrm{H} = \left[1 - \cos^2\alpha\sin^2\beta - \cos^2\alpha\sin^2\beta\tan^2\beta\right]$$

$$\mathrm{N} = \left[2 - \frac{\cos^2\alpha}{\cos^2\beta}\right]$$

The largest anticipated radial error in an ISM reconstruction, is found by calculating:

$$\delta R_{ISM} = R_{ISM}(\alpha - \delta\alpha, \beta + \delta\beta) - R_{ISM}(\alpha,\beta) \qquad (6)$$

Approximating an error sphere with δR_{ISM} lends a notion of the expected error in the ISM's reconstructed position, as a function of expected error bounds in $\delta\alpha$ and $\delta\beta$. This expression for δR_{ISM} also highlights another intuitive aspect of feature detection: the expressions that will appear in equation (6) will be both linearly and quadratically proportional to B, the size of the feature. This is interpreted to mean that the larger the feature is, the easier it becomes to detect it, but the greater the error in δR_{ISM}.

Once an error sphere is obtained, if three or less ISM centres are reconstructed such that their error spheres intersect and that those spheres have a smaller radius than the ISMs themselves, then there is a high probability that they belong to the same ISM. A weaker assumption is that any ISM centre reconstructions that are less than $\lambda/2$ units from each other, belong to the same ISM. These imposed constraints may be broken though, so that in a scenario where the errors in ISM centre reconstruction is large and an unknown number of ISMs has been captured in the image (for example due to lighting or structure occlusion), another approach can be adopted. The K-means clustering algorithm searches for *k* clusters in a group of points, through an iterative process (see Bishop[17]). This method can be used for trying to find the most suitable division of the centres, with the knowledge that no cluster can have more than 3 points belonging to it.

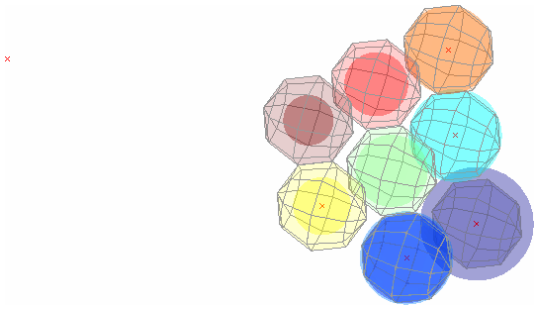

Figure 6: The camera origin (left) and centre estimates (right) are given by the red crosses, with the error spheres bounding them. The mesh spheres illustrate the relative size of an ISM. The larger error spheres are not due to their distance from the camera origin, but because of the higher eccentricity of some of the detected discs for that ISM. It should be noted that these are the worst-case error spheres.

Once the centre solutions are gathered into groups corresponding to the ISMs, the position estimate of that ISM centre can be found through the weighted average of these centre solutions, based on their corresponding error estimates. As a general rule, the larger and less eccentric the detected ellipse is, the smaller the corresponding error estimate.

When the positions of all the detected ISMs are obtained, one can implement equations that force the ISMs to obey a grid-like structure, fixing the distances and attitudes relative to each other. This is discussed in greater detail in our previous paper[14] and is not implemented for the results in the proceeding sections. We do, however, implement a simpler constraint that each ISM must be within at most $(1+\chi)\lambda$ to another ISM, where χ is chosen to reflect the confidence in the ISM structure reconstruction. This proves useful when the captured image contains a partially occluded disc. In such a situation, as the size of the disc is truncated, the ISM centre is reconstructed at a greater distance to the rest of the structure. The simple constraint given above allows obvious false solutions to be eliminated, but a more robust algorithm can be put in place to enforce that all ISMs must reconstruct in a relative structure, with a grid-like formation and aligned axes. RANSAC is a suggested method for finding the structure's estimated position and attitude and eliminating 'noisy' data, corresponding to inaccurate ISM centre solutions. A bonus (so to speak) of using such an algorithm is in detecting these outliers and identifying them as possible structure abnormalities: if the integrity of the structure is put into question, a RANSAC algorithm might correctly identify an ISM which has broken away from the structure. The cost of running such an algorithm, over the simple constraint described before, is in additional computation time.

Relative Attitude Estimation

This section describes the way the relative attitude of the ISMs is determined, using the feature detection method. We consider a scenario where a 3-by-3 structure is to be completed by adding a 9th ISM to the modules already connected, as shown in figure 4. The purpose is to determine the orientation of the incoming ISM that is attempting a docking manoeuvre, with respect to the ISM located at the centre of the structure.

This method uses a number of reflectors placed in an 'L-strip' form. Each line of this strip consists of 8 reflectors that would ease the identification of the ISM facet – see figure 7. The relative attitude is calculated from the relationship between the distances AC and BC. -See Table 1.

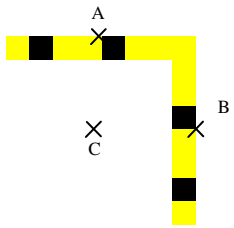

Figure 7: Configuration of the 'L' strip

The same image used by the position algorithm, described in the previous section, is processed to obtain the necessary information that would allow determining the relative attitude of the ISMs. For this purpose the following procedures are followed:

Initially the 'L' strips are detected and all the other features are removed from the image.

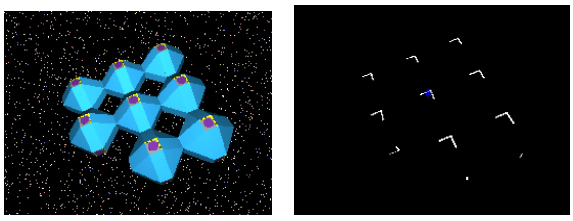

Figure 8: Original image (left) and the detected 'L' strips (right)

After position determination, the central ISM's corresponding disc is perspectively re-projected onto the image. The 'L' strip that corresponds to this facet is then selected for further processing. If more than one facet is visible (or the central ISM facets are not

detected), then the 'L' strip with the largest area is cropped.

Figure 9: The Selected 'L' Strip

Knowing the coordinates of the projected centre of mass, the algorithm provides the lengths AC and BC. At this end, the yaw, pitch and roll rotations are obtained. Table 1 depicts how the sides of the 'L' strip changes with the three rotations.

Table 1: The 'L' strip with the three rotations.

Rotation about	'L' strip	Rotation angle
x-axis	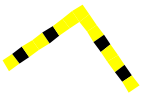	Roll (ψ)
y-axis		Pitch (φ)
z-axis		Yaw (θ)

Depending on the rotation performed, the 'L' strip takes different forms and its sides change in length. For pure pitch, the length AC takes a new value. For pure yaw, on the other hand, BC changes in length. Pure roll will result in rotating the 'L' strip and resizing neither AC nor BC.

In order to determine the true lengths AC_{true} and BC_{true}, this algorithm requires the relative distance between the centre of the central ISM (of the 3x3 structure) and the ISM to be added to this structure. This relative distance is obtained from the position determination algorithm, described in the previous section. Knowing this relative distance, the axial distance between the camera and the facet of the selected 'L' strip is deduced. Thus the true lengths AC_{true} and AB_{true} are calculated by obtaining the pixel resolution of the camera.

The pixel size is a function of the field of view of the camera $f.o.v$, the relative distance between the camera and the detected facet d' and the number of pixels in the camera string px :

$$pixel_{res} = \frac{2d' \tan(\frac{f.o.v}{2})}{px} \tag{7}$$

In this document we selected the (3, 2, 1) rotation about the x-axis, then the rotated y-axis, and finally about the new z-axis.

The roll angle is estimated by defining the rotation of the 'L' strip on the image plane.

For pitch rotation, only AC rotates on the XZ plane and therefore the pitch angle is defined using:

$$\cos\varphi = \frac{AC_{new}}{AC_{true}} \tag{8}$$

Similarly, for yaw the side BC rotates about the XY plane, leading to estimating the yaw rotation from:

$$\cos\theta = \frac{BC_{new}}{BC_{true}} \tag{9}$$

Where AC_{true} and BC_{true} denote the lengths AC and BC as they would appear on the image plane, if there were no rotations (at a particular distance). At the same separation distance and when the ISM rotates, AC and BC take the lengths AC_{new} and BC_{new} .

Because of the cosine trigonometry, the angle obtained may give +/- the right angle of rotation. A way to solve this issue is to define the location of crossing point of the 'L' strip sides. Knowing this location with respect to the points A and B, as well as identifying the ISM side the camera is facing, allows to choose between the plus and minus solutions.

RESULTS

Result Formulation and Error Functions

The freeware program POVRay[18] for Windows v. 3.6 was used to generate the images, in conjunction with MATLAB to process the images and run the algorithms derived in the previous sections. The camera setting for POVRay creates a 600x800 (rows by columns) image, with a focal length of 1 millimetre and a field of view of 90^ox120^o – a wide field of view. The calculations for finding the effects that these camera specifications have on the accuracy of the reconstructions are now shown,

starting with the field of view and ending with the resolution.

In the worst-case scenario, the semi-major and semi-minor axes of the ellipses (used for position determination) are obtained with a +/- ½ pixel ambiguity, when considering the planar projection. If there are *m* pixels in a column, then the error δa in the semi-major axis of the planar ellipse is given by

$$\delta a = \frac{\tan\left(\frac{f.o.v.}{2}\right)}{m} \tag{10}$$

In the worst-case, the ellipse is centred along the focal axis, in which case the relationship between the planar ellipse semi-major axis and the spherical ellipse semi-major axis is given by

$$a = \tan(\alpha) \tag{11}$$

Therefore, an error of δa in the planar ellipse semi-major axis corresponds to an error $\delta\alpha$ in the spherical ellipse semi-major axis as:

$$\tan(\alpha + \delta\alpha) = a + \delta a = \tan(\alpha) + \delta a \tag{12}$$

Solving for $\delta\alpha$, we obtain an expression for use in equation (6):

$$\delta\alpha = \arctan\left(\frac{\tan\left(\frac{f.o.v.}{2}\right)\cos^2\alpha}{m - \sin\alpha\cos\alpha}\right) \tag{13}$$

Likewise, the expression holds when replacing $\delta\alpha$ with $\delta\beta$ and α with β. In figure (6) the error spheres were shown for a camera with specifications given at the beginning of this section. If the camera is replaced by one with an f.o.v. of 25°, the error spheres become roughly one fifth of their original radius. In general, this means that the errors found in the ISM positions can be divided by 5.

We can also calculate, in a qualitative manner, the effects of reducing the field of view to the accuracy of the overall attitude estimate of the ISM structure. If l describes the 'orthographic projection' length of a reflector strip, at a distance d_i away from the camera, then the arc-length η_i which its projection onto an image sphere makes, is given by

$$\tan(\eta_i) = \frac{l}{d_i} \tag{14}$$

Any pose estimate $\vec{p}$ will have an associated change, with a corresponding change in d_i:

$$\Delta\vec{p} = \frac{\delta\vec{p}}{\delta l}\Delta d = \frac{\delta\vec{p}}{\delta l}(d_2 - d_1) = \frac{\delta\vec{p}}{\delta l}d_1\left(\frac{\tan\eta_1}{\tan\eta_2} - 1\right) \tag{15}$$

If the minimum detectable change in η is denoted $\Delta\eta$, then

$$\Delta\vec{p} = \frac{\delta\vec{p}}{\delta l}d_1\tan(\Delta\eta)\left(\frac{1 + \tan 2\eta_1}{\tan\eta_1 + \tan(\Delta\eta)}\right) \tag{16}$$

This implies that the magnitude of errors inflicted on pose estimates is proportional to $\tan(\Delta\eta)$ (assuming that η is much larger than $\Delta\eta$). In terms of the f.o.v., if the camera projection was directly onto a sphere, then $m\Delta\eta = f.o.v.$. But, for suitably small fields of view, this approximation still holds in the planar projection case. As such, equation (16) implies that errors obtained in the attitude estimates, are proportional to the tangent of the f.o.v.. For example, reducing the f.o.v. from 90° to 25° will give an attitude estimate that is 3.6 times more accurate.

Finally, at present, a high-resolution CMOS camera can have up to 14 Megapixels[19] – around 5 times the quality of the 600x800 pixel images we consider. This would correspond to the same level of error, if we were at 5 times the distances considered, but at an increased mass budget, power consumption, size and image processing time.

All the results generated assume a 600x800 image with a 90° f.o.v.. Accuracy should be scaled, according to the camera specifications chosen.

Simulation Results

A specific ISM structure was considered, for the purposes of testing the position and attitude determination techniques described in the previous sections. The structure consists of 8 ISMs in a 3x3 lattice, with one ISM missing. The images generated mimic those which might be seen from the 9th ISM on its final docking trajectory. Figure 10 displays the aforementioned structure with the axes of the structure frame highlighted.

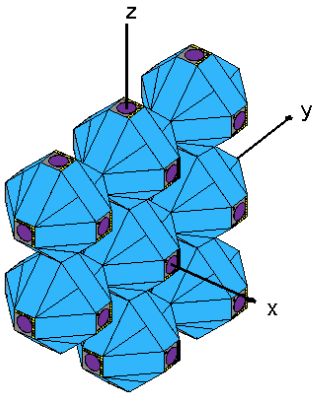

Figure 10: The ISM structure considered. The axes are defined so that the missing ISM slot is in the negative y and z position.

Define the camera frame to be centred at the focal point of the camera, with its *x*-axis aligned with the focal axis and *y*-axis and *z*-axis aligned with the rows and columns of the captured images respectively. Define the structure frame to have its centre co-aligned with the central ISM, with the x-axis pointing out of the plane containing all of the ISM centres. The y-axis and z-axis are aligned with the primary EFDS facets of the ISMs. The missing ISM centre would lie at $[0,-\lambda,-\lambda]$ in the structure frame, where λ is the distance between ISM centres.

We define $R(\theta,\varphi,\psi)$ as the rotation from the structure's body-axes to the camera's axes. The rotations in R are a 3-2-1 rotation: first a rotation θ about the *z*-axis, followed by a second rotation φ about the rotated *y*-axis and finally a third rotation ψ about the rotated *x*-axis. Ergo, by denoting *cos* with *c* and *sin* with *s*, we define

$$R = \begin{pmatrix} c\theta c\varphi & c\theta s\varphi s\psi + s\theta c\psi & -c\theta s\varphi c\psi + s\theta s\psi \\ -s\theta c\varphi & -s\theta s\varphi s\psi + c\theta c\psi & s\theta s\varphi c\psi + c\theta s\psi \\ s\varphi & -c\varphi s\psi & c\varphi c\psi \end{pmatrix} \qquad (17)$$

Two sets of simulations were considered: varying radial distance to the target structure and varying the rotation of the structure relative to the camera. In the first set of simulations, the radial distance was varied from 2m to 10m and the ISM structure centre remained on the focal axis. The fixed rotation was defined with $\theta = 30^{o}$, $\varphi = 10^{o}$ and $\psi = 20^{o}$. The closest image is given in figure 11(a) and the farthest image is given in figure 11(b)/(c).

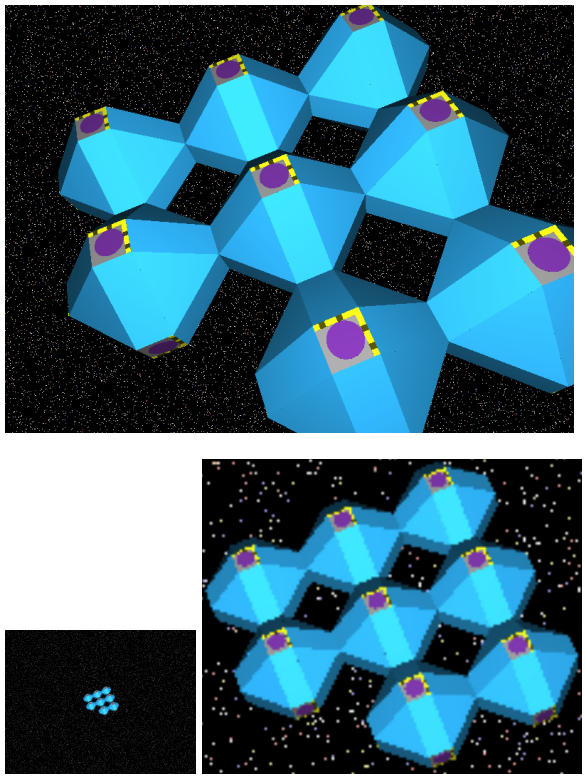

Figure 11: Simulations included examining the radial variation in accuracy. The closest relative position (11(a) – top) was at 2m, the farthest (11(b) – bottom left) at 10m. When magnified (11(c) – bottom right), the pixellation becomes clearer.

The accuracy in position estimates is given in figure 12. In each reconstruction, the ISM centres that were reconstructed were matched with the ISMs in the 3D model. Out of each ISM that was reconstructed, the maximum error was plotted (black curve), along with the average positional error (blue curve).

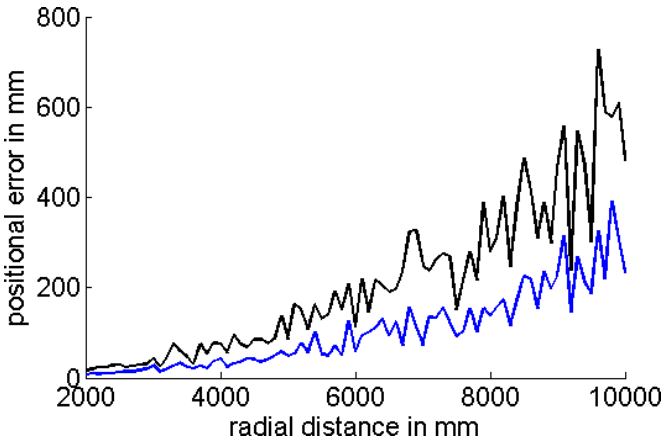

Figure 12: Illustrating the positional error as the structure's radial distance from the camera is varied.

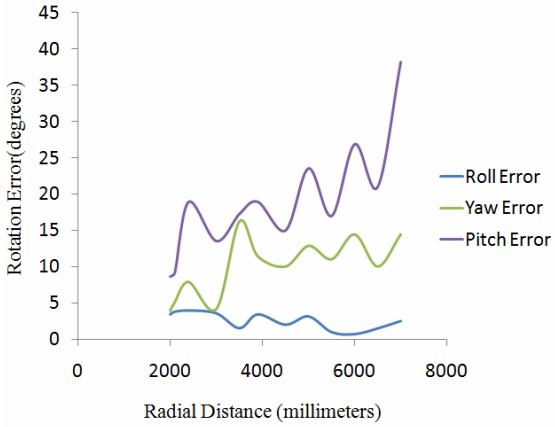

Figure 13: Illustrating the rotational error as a function of the radial distance

Figures 13 depicts the measurement errors in yaw, pitch and roll, as a function of the docking ISM position. As the relative distance between the middle ISM of the constructed structure and the ISM docking with this structure increases, the accuracy in measurement decreases. This is due to the fact that at larger distance the lengths AC and BC (described in section 3) occupy fewer pixels. Therefore measuring these lengths becomes less accurate.

In the second set of simulations, the radial distance from the camera to the centre of the ISM structure was fixed at 3m, with the relative orientation cycling through rotations of θ and φ, with a step-size of 10^{o} in each axis. The resulting error surfaces for the position determination are shown in figure 13. As described for the radially varying scenario, both the maximum and average positional errors were captured. The average error would in general stay at around 20-40mm. However, we notice from the results that 5 sharp peaks occur in the errors. This is a result of partial occlusion, as discussed in the position determination section. Though larger errors were averted, without implementing a more rigorous ISM grid-constraint, such false readings can occur, as demonstrated in figure 14.

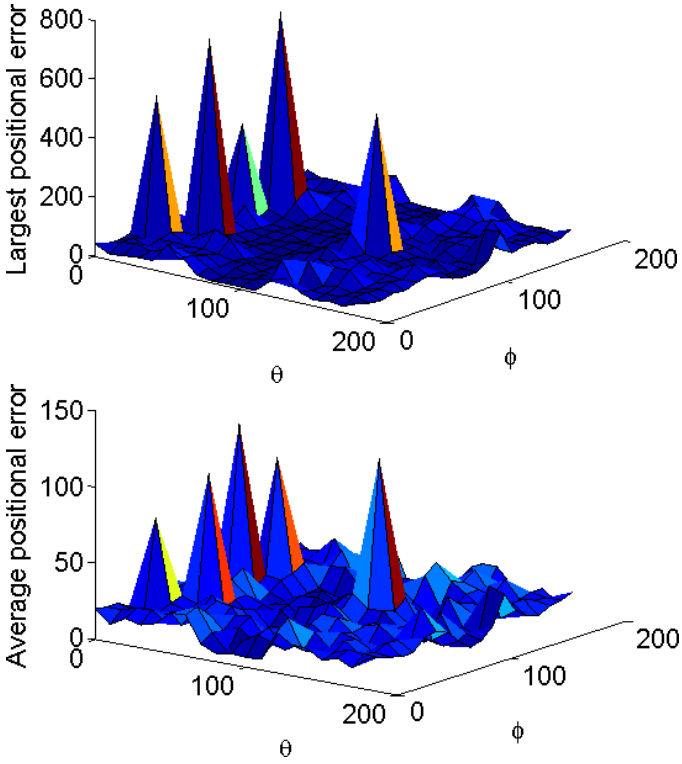

Figure 14: Illustrating the maximum (13(a) - top) and minimum (13(b) - bottom) error in position for a fixed relative position, when the rotation of the ISM structure is varied.

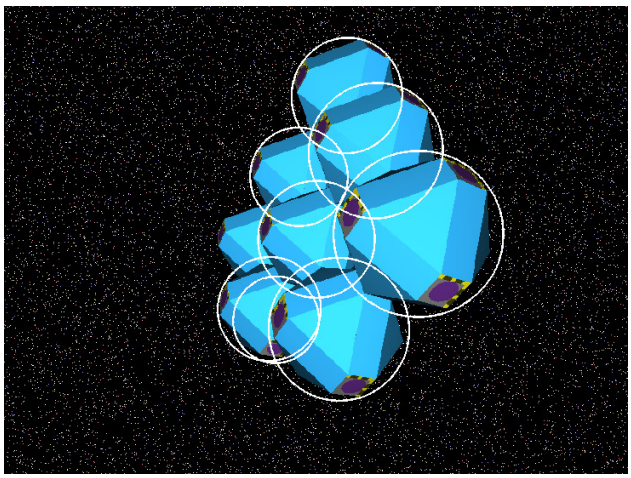

Figure 15: Partial occlusion can lead to false readings, without more stringent constraints placed on the pose reconstruction of the ISMs, relative to each other.

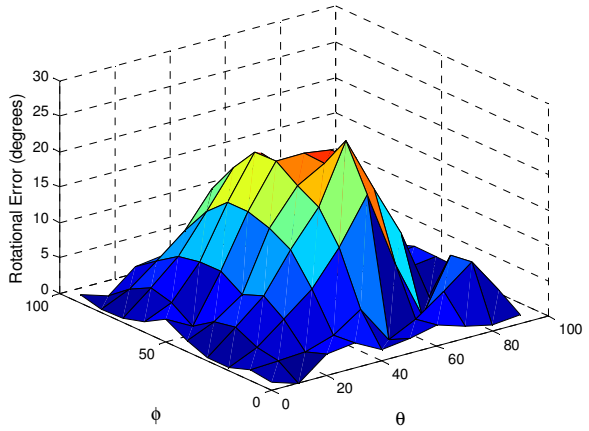

Figure 16: Rotational Error in degrees

Figure 16 shows the error measurements when the yaw and pitch rotations cycle between 0 and 90º. As depicted, the maximum errors occur in the range [40º 60º]. The graph is roughly symmetric, about the rotation angles of 45º for both angles.

CONCLUSION

An algorithm for determining the relative position and orientation of a neighbouring ISM structure has been identified. Using two specific features to assist in each stage, the positional accuracy is found to within 20mm at 3m and within 600mm at 10m. The relative attitude is found to within 10^{o} at 2m and within 25^{o} at 6m. The algorithms developed have been tested on a relatively complex structure, but will also hold for any generic structure. Furthermore, the scenarios can be generalized further to multiple ISM structures without much development required.

The algorithm that detects the features of the 'L' strip of reflectors provides acceptably accurate measurements of the orientation of the ISM, considering the large field of view that was used. As the ISM is dependent on the electromagnetic forces to complete physical coupling, very high accuracy and precise alignment is not crucial.

In the expected mission confines, there would just be one ISM structure to be docked with; hence a single pose estimate is all that is required. In such a scenario a narrower field of view is recommended, leading to faster calculation times (less facets to reconstruct) and greater accuracy.

ACKNOWLEDGEMENTS

The authors would like to thank several students at the Surrey Space Centre, including members of the Astrodynamics Group for their ideas and suggestions, along with the U26 students for their contributions. They are, as always, appreciated.

The primary author would also like to thank UKRC for their financial support for attending the Utah conference and presenting this research.

REFERENCES

[1]Esper, J., Andary, J., Oberright, J., So, M., Wegner, P., Das, A., et al. (2004). Modular, Reconfigurable, and Rapid Responsive Space Systems: the Remote Sensing Advanced Technology Microsatellites. *2nd Responsive Space Conference.* Los Angeles, CA, USA.

[2]*Mir Orbital Complex Content*. Retrieved May 25, 2009, from S. P. Korolev RSC Energia: http://www.energia.ru/english/energia/mir/mir-structure.html

[3]Chabert, F. (2002). Automatic Transfer Vehicle (ATV) GNC overview. *34th COSPAR Scientific Assembly, The Second World Space Congress.* Houston, TX, USA.

[4] *A brief Description of the Radar Approach Equipment of the Soyuz-Type Spacecraft.* Washignton DC: NASA Technical Translation. (1970)

[5]Hinman, E. M., & Bushman, D. M. (1991). *Soviet Automated Rendezvous and Docking System Overview.* NASA Automated Rendezvous and Capture Review. N93-21407 07-12.

[6]Bryan, T. C., Howard, R., Johnson, J. E., Lee, J. E., & Spencer, S. H. (2008). Next Generation Advanced Video Guidance Sensor. *IEEE Aerospace Conference* (pp. 1-8). Montana: IEEE.

[7]Mitchell, J. D., Cryan, S. P., Strack, D., Brewster, L. L., Williamson, M. J., Howard, R. T., et al. (1-16). Automated Rendezvous and Docking Sensor Testing at the Flight Robotics Laboratory. *IEEE Aerospace Conference* (2007). Montana: IEEE.

[8]Weismuller, T., & Leinz, M. (2006). GN&C Technology Demonstrated by the Orbital Express Autonomous Rendezvous and Capture Sensor System. *29th Annual AAS Guidance and Control Conference.* Breckenridge, Colorado: American Astronautical Society.

[9]Pinard, D., Reynaud, S., Delpy, P., & Strandmoe, S. E. (2007). Accurate and Autonomous Navigation for the ATV. *Aerospace Science and Technology , 11*, 490-498.

[10]Smail, S., & Underwood, C. I. (2009). Electromagnetic Flat Docking System for In-Orbit Self-Assembly of Small Spacecraft. *AAS/AIAA Spaceflight Mechanics Meeting.* Savannah, Georgia, USA.

[11]Cock, F. H., & Watkins, S. (1993). *Magnetic Shielding of Interplanetary Spacecraft against Solar Flare Radiation.* NASA/USRA Advanced Design Program. NASA-CR-2 95539.

[12]Ruilier, C., Krawczyk, R., Sghedoni, M. M., Chanal, O., Degrelle, C., Pirson, L., et al. (2007). System Assessment Study of the ESA Darwin Mission: concepts trade-off and first iteration design on novel Emma arrangement. *SPIE , 6693*, 66930T-66930T-10.

[13]SBSP Group (2007). *Space-Based Solar Power As an Opportunity for Strategic Security.* National Security Space Office Interim Assessment.

[14]Wokes, D. S., Smail, S., Palmer, P. L., & Underwood, C. I. (2009). Pose Estimation for In-Orbit Self-Assembly of Itelligent Self-Powered Modules. *AIAA Guidance, Navigation and Control Conference and Exhibit.* Chicago, Illinois, USA.

[15]Semple, J. G., & Kneebone, G. T. (1952). *Agebraic Projection Geometry.* London: Oxford at the Clarendon Press, Oxford University Press, Amen House, London E.C.4.

[16]Wokes, D. S. and Palmer. P. L., "Perspective Projection of A Spheroid Onto An Image Sphere," *SIAM Journal on Imaging Science* (Pending publication).

[17]Bishop, C. M. (1996). *Neural Networks for Pattern Recognition*, Oxford University Press, 1st edition, USA. ISBN: 0198538642.

[18]Persistence of Vision Raytracer Pty.Ltd. *Persistence of Vision Raytracer (POVRay).* Retrieved June 8, 2009, from http://www.povray.org

[19]C-Cam Technologies. *High Resolution CMOS Camera*. Retrieved June 7, 2009, from http://www.latronix.se/pdf/kameror/FCi4-14000.pdf